AGU PUBLICATIONS

Global Biogeochemical Cycles

RESEARCH ARTICLE
10.1002/2015GB005251

Key Points:
- Explicit inclusion of bubble injection is required for oxygen flux calculations
- Winter oxygen flux estimates are key to resolving annual net community production
- Winter heterotrophy can significantly reduce production determined from summer measurements

Supporting Information:
- Text S1 and Figure S1
- Data Set S1

Correspondence to:
S. M. Bushinsky,
sb17@princeton.edu

Citation:
Bushinsky, S. M., and S. Emerson (2015), Marine biological production from in situ oxygen measurements on a profiling float in the subarctic Pacific Ocean, *Global Biogeochem. Cycles*, *29*, doi:10.1002/2015GB005251.

Received 26 JUL 2015
Accepted 8 NOV 2015
Accepted article online 10 NOV 2015

Marine biological production from in situ oxygen measurements on a profiling float in the subarctic Pacific Ocean

Seth M. Bushinsky[1] and Steven Emerson[1]

[1]School of Oceanography, University of Washington, Seattle, Washington, USA

Abstract Evaluating the organic carbon flux from the surface ocean to the interior (the marine biological pump) is essential for predictions of ocean carbon cycle feedback to climate change. One approach for determining these fluxes is to measure the concentration of oxygen in the upper ocean over a seasonal cycle, calculate the net O_2 flux using an upper ocean model, and then use a stoichiometric relationship between oxygen evolved and organic carbon produced. Applying this tracer in a variety of ocean areas over seasonal cycles requires accurate O_2 measurements on autonomous vehicles. Here we demonstrate this approach using an O_2 sensor on a profiling float that is periodically calibrated against atmospheric pO_2. Using accurate data and a model that includes all physical and biological processes influencing oxygen, we determine an annual net community production of 0.7 ± 0.5 mol C m^{-2} yr^{-1} in the northeast Pacific Ocean (50°N, 145°W) from June 2012 to June 2013. There is a strong seasonal cycle in net biological oxygen production with wintertime fluxes caused by bubble processes critical to determining the annual flux. Approximately 50% of net autotrophic production during summer months is consumed by net respiration during the winter. The result is a biological pump in the subarctic Pacific Ocean that is less than that determined by similar methods in the subtropics to the south. This estimate is significantly lower than that predicted by satellite remote sensing and global circulation models.

1. Introduction

Net carbon export from the upper ocean draws CO_2 from the atmosphere to the ocean and fuels respiration in the aphotic deep sea [e.g., *Toggweiler and Sarmiento*, 1985; *Volk and Liu*, 1988]. While ocean climate models predict that feedback to the future levels of atmospheric pCO_2 caused by changes in the annual net carbon production (ANCP) should be of second order [*Bopp et al.*, 2013], climate induced changes in the biological pump will have an important influence on the distribution and stability of the oxygen minimum zones of the ocean [*Hofmann and Schellnhuber*, 2009; *Kwon et al.*, 2009]. The location and intensity of low oxygen concentrations are important for the survival of benthic organisms and greatly influence the nitrogen cycle [*Altabet*, 2007; *Diaz and Rosenberg*, 2008].

There have been several recent attempts to use satellite remote sensing to determine the global distribution of the biological pump [*Laws et al.*, 2011; *Westberry et al.*, 2012; *Siegel et al.*, 2014]. Net biological carbon export determined in this way is often used as the boundary condition for the biogeochemical component of climate models [*Yool et al.*, 2013]. The remote sensing-based methods predict strong geographic variability in the biological pump—variations of at least a factor of 4 between the subtropical lows and higher values in the equator and subarctic latitudes [*Laws et al.*, 2011; *Westberry et al.*, 2012]. Verifications of the satellite-determined carbon export have been attempted locally but are limited to select locations where it has been possible to do time series studies of upper ocean mass balances of carbon, oxygen, and nutrients [*Juranek et al.*, 2012; *Emerson*, 2014]. A compilation of annual organic carbon export estimates by mass balance methods indicates that they range between 2 and 4 mol C m^{-2} yr^{-1} in the open ocean with no clear latitudinal dependence (see *Emerson* [2014], Table 2), but with near-shore values that are about twice this [*Munro et al.*, 2013].

It is unresolved whether satellite-predicted carbon export values are more variable than reality or if the experimental results are simply too few to capture true ocean variability. This conundrum can be solved by a much broader distribution of ANCP determinations, but it must be done primarily by in situ measurements on autonomous platforms because of the great expense of ship-based annual time series measurements.

Long-term, in situ measurements are required to resolve the spatial and temporal variability in ANCP [*Westberry et al*., 2012]. A method of achieving these ends is instrumenting profiling floats and gliders with oxygen sensors [*Gruber et al*., 2009; *Johnson et al*., 2009]. Only a few studies of upper ocean oxygen mass balance have been done this way [*Nicholson et al*., 2008; *Riser and Johnson*, 2008; *Fiedler et al*., 2013], however, because of accuracy issues with autonomous oxygen sensors. Calibration drift [*D'Asaro and McNeil*, 2013] has necessitated in situ calibration of oxygen sensors in order to achieve sufficient accuracy for determining air-sea oxygen fluxes. Aanderaa optodes, the sensors currently used most frequently on autonomous vehicles, are more stable in the field than in the lab, but few long-term calibrations of deployed sensors have been conducted to establish stability at the accuracy needed to resolve air-sea gas exchange [*Takeshita et al*., 2013; *Emerson and Bushinsky*, 2014].

Open ocean surface oxygen concentrations depart by only a few percent from atmospheric equilibrium [e.g., *Emerson et al*., 2008] requiring accuracies on the order of ± 0.2–0.4% (~0.5–1 μmol kg^{-1}) to determine air-water exchange fluxes. We achieve these accuracies by calibrating the Aanderaa optodes in the laboratory as a function of temperature and oxygen concentration and then calibrating them in situ against atmospheric pO_2 to determine the air-water difference in pO_2 when the floats surface after collecting ascending profiles of T, S, and O_2. Performing multiple calibrations may eventually prove to be unnecessary, but the most important part for long-term data interpretation will be the in situ atmospheric calibrations [*Bittig and Körtzinger*, 2015]. Much of the calibration procedure is described elsewhere [*Bushinsky and Emerson*, 2013; *Emerson and Bushinsky*, 2014; S. M. Bushinsky et al., Accurate oxygen measurements on modified Argo floats using in situ air calibrations, submitted to *Limnology and Oceanography: Methods*, 2015].

We present a seasonal cycle of oxygen data from a profiling float deployed near Ocean Station Papa (OSP, 50°N × 145°W). OSP is a time series site with a long history of O_2 measurements and prior mass balance estimates of C export. Production in the region is controlled by light and iron availability resulting in a strong seasonal cycle. We solve the problem of accuracy by in situ calibration of the sensor against the atmosphere and show that these data can be interpreted in terms of annual net community production and biological carbon export. It should now be possible to apply this method widely to many ocean locations and, together with satellite-determined remote sensing, evaluate the global geographic distribution of the biological pump and its evolution with time.

2. Methods

2.1. Optode Calibration and Float Deployment

Oxygen concentrations were determined using an Aanderaa optode sensor on a ~60 cm long polyether ether ketone pole attached to the end cap of an Argo float (UW float ID: 8397 and World Meteorological Organization ID: 5903743) constructed at the University of Washington. This insures that the optode will measure purely atmospheric pO_2 rather than a mixture of surface ocean and atmosphere because of being splashed by surface ocean water. Firmware is adjusted to make oxygen measurements every 2 min for 1 h when the float is at the surface.

The Aanderaa optode (model 4330) was calibrated in the laboratory at atmospheric pressure across nine oxygen saturations (0–115%) and five temperatures (1–21°C). The calibrated sensor was then exposed to a moist atmosphere of known pressure to check for differences in sensitivity in water and air. Within the errors of our measurements the sensor accuracy is identical in air and water. Details of these tests are presented in *Bushinsky and Emerson* [2013] and S. M. Bushinsky et al. (submitted manuscript, 2015).

After deployment, air measurements of atmospheric pO_2 after each profile were compared to expected atmospheric pO_2 derived from National Center for Environmental Prediction (NCEP) reanalysis data to provide an initial calibration point (S. M. Bushinsky et al., submitted manuscript, 2015) (supporting information). The track of the O_2-Argo float and measured oxygen supersaturation (ΔO_2) as a function of depth is indicated in Figure 1. Winkler samples were taken from CTD casts after each of the first four profiles, and measured [O_2] agreed (to within 0.3%) with optode oxygen calibrated to air measurements. A long-term drift of -0.5%/yr was determined from the air measurements and used to perform a linear drift correction of the oxygen data (Figure S1 in the supporting information). Air measurements were only used from periods of stable atmospheric conditions, as determined from rates of temperature, pO_2, and atmospheric pressure change (see supporting information). A 1.5 year comparison of oxygen supersaturation with the nearby OSP mooring

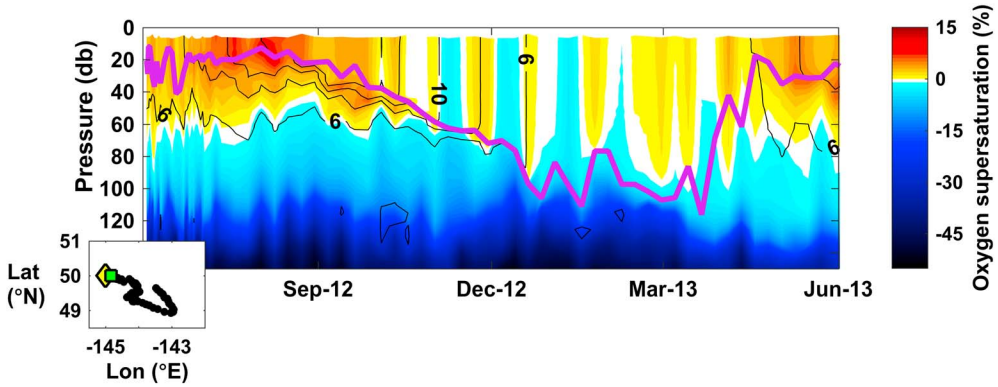

Figure 1. Oxygen supersaturation, ΔO_2 (%) = $([O_2] - [O_2]_{sat}/[O_2]_{sat}) \times 100$, as a function of depth and time in the northeastern subarctic Pacific. The heavy line represents the mixed layer depth using a 0.2°C potential temperature change from 10 m [*de Boyer Montégut et al.*, 2004]. Lighter lines are constant temperature contours, and colors are ΔO_2. The float track for the oxygen data presented in the inset shows the initial deployment (green square) and the position of the OSP mooring (yellow diamond).

(independently calibrated against ship-based Winkler samples) confirmed final drift-adjusted calibration [*Emerson and Bushinsky*, 2014].

2.2. Upper Ocean Oxygen Mass Balance Model

The mass balance of oxygen in the mixed layer (mol O_2 m^{-2} d^{-1}) is controlled by air-water exchange, $F_{A\text{-}W}$, horizontal and vertical advection, F_H and F_ω, entrainment of waters below the mixed layer, F_E, vertical mixing, $F_{\kappa z}$, and net biological oxygen production (or consumption), J_{O_2} [*Emerson and Stump*, 2010]:

$$\frac{d(h[O_2])}{dt} = F_{A\text{-}W} + F_H + F_\omega + F_E + F_{\kappa z} \pm J_{O_2} \quad (1)$$

Brackets indicate concentration (mol m^{-3}), and h (m) is the depth of the mixed layer determined by the vertical density profile derived from float temperature and salinity measurements [*de Boyer Montégut et al.*, 2004]. Each of the terms on the right-hand side of the above equation, except for J_{O_2}, is expanded into its component terms consisting of a mass transfer coefficient, advection velocity, or eddy diffusion coefficient times the oxygen concentration or concentration gradient.

The abiotic upper ocean model compartmentalizes the upper 150 m of the ocean into a variable height mixed layer box with 1.5 m boxes below (Figure 2), in which equation (1) is solved for all the terms except J_{O_2}. Box height was set to 1.5 m to allow model runs using large diapycnal diffusivity coefficients (high rates of diffusion require small box sizes or short time steps). Mixed layer depth and gas solubility [*García and Gordon*, 1992] (Benson and Krause coefficients) are determined from float measured temperature and salinity. In this way we derive an "abiotic oxygen" distribution that is stepped forward in time from the initial condition determined by the measured O_2 profile just after deployment in June. The bottom oxygen boundary at 150 m is set to the measured oxygen gradient at that depth, and the model solves for the concentration at 150 m. Calculated ANCP is not sensitive to changing the bottom boundary depth or to using the measured gradient instead of the measured oxygen concentration. The abiotic oxygen flux is calculated every 3 h from each physical term ($F_{A\text{-}W}$, F_H, F_ω, F_E, and $F_{\kappa z}$). Net biological oxygen production is equal to the difference between the measured (subscript M) and calculated (subscript C) terms:

$$\left.\frac{d(h[O_2])}{dt}\right|_M - \left.\frac{d(h[O_2])}{dt}\right|_C = (F_{A\text{-}W_M} - F_{A\text{-}W_C}) + (F_{H_M} - F_{H_C}) + (F_{\omega_M} - F_{\omega_C}) + (F_{E_M} - F_{E_C}) + (F_{\kappa z_M} - F_{\kappa z_C}) \pm J_{O_2} \quad (2)$$

where $d(h[O_2])/dt$ represents the change in oxygen concentration for each box at each time step. Each flux term is described below.

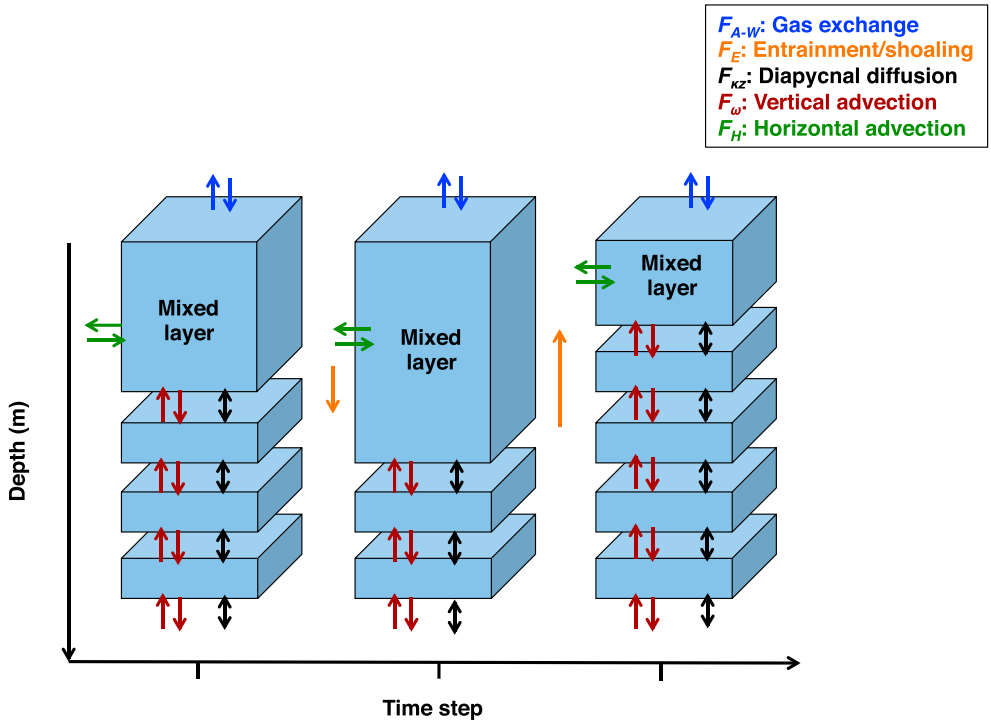

Figure 2. Schematic showing three time steps with the mixed layer deepening and shoaling between time steps. $F_{A\text{-}W}$ (air-water gas exchange, blue arrows) and F_H (horizontal advection, green arrows) are calculated for the mixed layer only. F_E (entrainment/shoaling, orange arrows) redistributes oxygen between boxes but results in no column-integrated change in the oxygen inventory. F_ω (vertical advection, red arrows) moves oxygen according to uniform Ekman velocities calculated from satellite-derived wind stress and the oxygen difference between adjacent boxes. F_{kz} moves oxygen between all boxes according to the diapycnal eddy diffusivity coefficient and the oxygen gradient.

2.2.1. $F_{A\text{-}W}$: Air-Sea Gas Exchange

Air-water exchange is modeled as the sum of diffusive interface exchange, F_S, and transport by bubbles due to breaking waves, F_B:

$$F_{A\text{-}W} = F_S + F_B \tag{3}$$

Multiple air-sea gas flux parameterizations were compared to N_2 data derived from a Gas Tension Device deployed at OSP (see *Emerson and Stump* [2010] for description of N_2 determined from these measurements). The best fit to the N_2 data was derived using the model of *Liang et al.* [2013], which explicitly separates diffusive gas exchange, large bubbles that exchange with water, and small bubbles that collapse and inject all of their gas into the water (Figure 3). The diffusive component is the product of a mass transfer coefficient (k) times the measured or modeled surface concentration ($[C]$) difference from saturation ($[C]_{sat}$) calculated using measured T and S:

$$F_S = k\left([C] - [C]_{sat}\right) \tag{4}$$

where k is a function of wind speed and Schmidt number. Transport by bubbles ($F_B = f(U_{10}, \Delta_P)$) is divided into small bubbles, which are purely a function of wind speed (U_{10}), and large bubbles, which get driven deeper at higher wind speeds, increasing the effective gas solubility through increased hydrostatic pressure (Δ_P) [*Liang et al.*, 2013]. Both small and large bubbles play a large role in the wintertime influx of oxygen.

2.2.2. F_H: Horizontal Advection

Horizontal advection is calculated for the mixed layer box using World Ocean Atlas climatological gas saturation [*Kalnay et al.*, 1996; *Garcia et al.*, 2010] and NCEP reanalysis surface currents. Saturation differences between the float location and source waters determined by current speed are used to calculate oxygen flux. Because climatological data includes biological effects, horizontal advection fluxes are used in the abiotic model to determine gas evolution ($d(h[O_2])/dt_C$) but not when determining the difference between abiotic

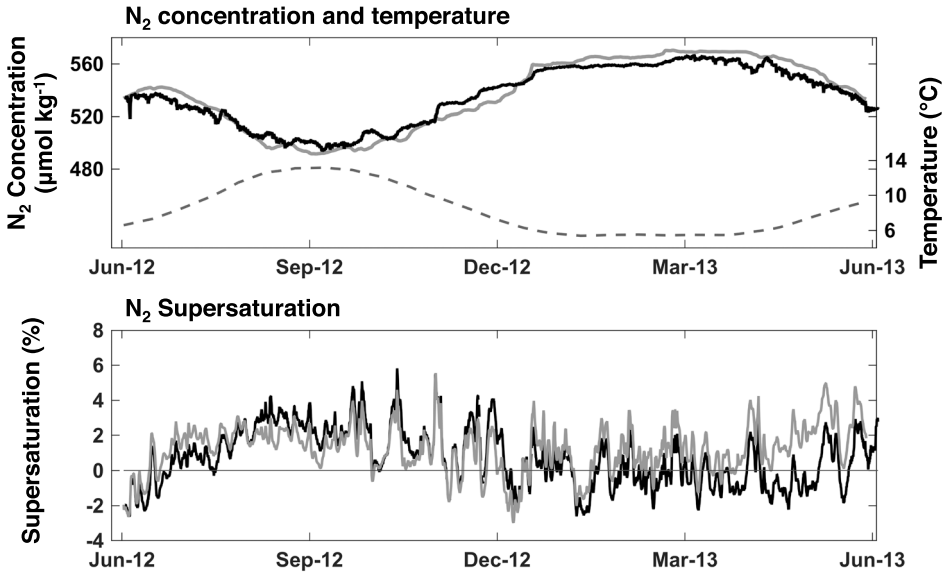

Figure 3. (top) N_2 concentration and Ocean Station Papa temperature and (bottom) N_2 saturation. Data (black lines) are calculated from total gas pressure measured by a Gas Tension Device. Temperature (dashed gray line) is measured from a SeaBird Electronics 16 Plus conductivity, temperature, and depth sensor. Modeled data (gray lines) are from the one-dimensional abiotic gas model using the *Liang et al.* [2013] gas parameterization.

and biotic fluxes ($F_{H_M} - F_{H_C}$ is assumed to be zero). This is an approximation, but the magnitude of the horizontal advective flux is small relative to calculated ANCP.

2.2.3. F_ω: Vertical Advection

To calculate the vertical advective flux, Ekman pumping (suction) velocities [*Hartmann*, 1994] were calculated from Advanced Scatterometer-derived wind stress fields [*Bentamy et al.*, 2008]. The flux of oxygen due to Ekman pumping was calculated in the direction of the flow by multiplying the velocity times the concentration difference between two adjoining boxes.

2.2.4. F_E: Entrainment

Entrainment is the rate of deepening of the mixed layer (h_E) times the vertical gradient in gas concentration. In the model, this is represented by a flux of oxygen between the mixed layer and the box below

$$F_E = [C]\rho h_E \tag{5}$$

If the mixed layer is deepening and entraining water below, [*C*] is the concentration and ρ is the density of the box below the mixed layer. If the mixed layer is shoaling, oxygen is added to the box below and [*C*] and ρ are mixed layer concentration and density. F_E for the mixed layer and the box below are of equal magnitude and opposite sign. This redistributes gas between the mixed layer and the water below but results in no net gas flux once integrated to the deepest depth of the seasonal mixed layer.

2.2.5. $F_{\kappa z}$: Diapycnal Eddy Diffusion

The diapycnal eddy diffusion flux between the top and bottom of each box is calculated as a function of the diapycnal diffusivity coefficient (κ_z) times the concentration gradient between boxes. Diffusivity at the base of the mixed layer, defined as the 20 m depth interval below the mixed layer depth, calculated from heat and salt balances derived from a surface mooring, seaglider, and profiling floats at OSP [*Cronin et al.*, 2015] indicates a seasonal cycle in κ_z with a

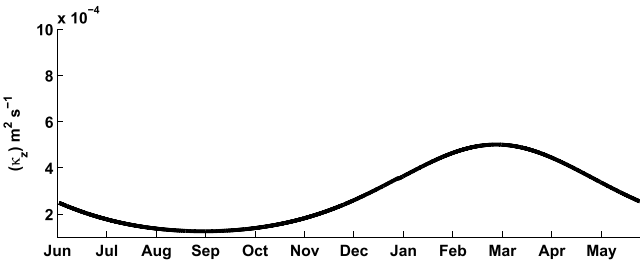

Figure 4. Seasonal variation in the diapycnal eddy diffusion coefficient (κ_z) at the base of the mixed layer used in the abiotic model. The magnitude, amplitude, and seasonal cycle were chosen to best fit the κ_z climatology from heat and salt budgets calculated at OSP [*Cronin et al.*, 2015].

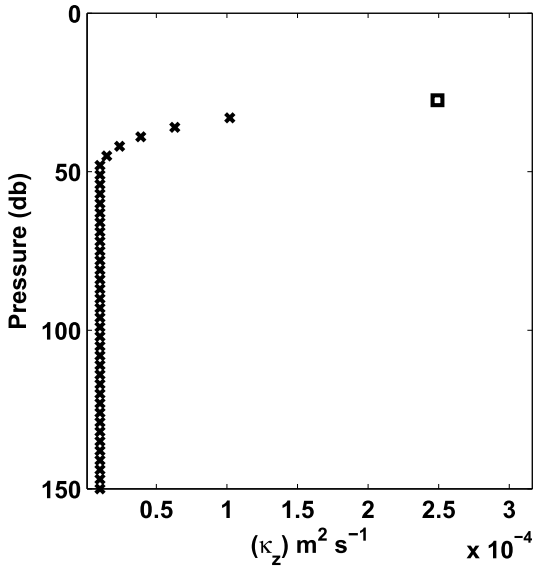

Figure 5. Example of the diapycnal diffusivity coefficient (κ_z) profile with depth from June 2012. κ_z for diffusion between the mixed layer and the box below (square) is determined by the seasonal cycle shown in Figure 4. The diffusivity coefficients for deeper boxes (crosses) follow an exponential decay over 20 m [*Sun et al.*, 2013] to the background value of $\kappa_z = 10^{-5}\,m^2\,s^{-1}$.

maximum in April and a minimum in October. We used a seasonally varying κ_z that fell in between the heat- and salt-derived κ_z climatologies presented in *Cronin et al.* [2015] (Figure 4). κ_z decreases with depth from the base of the mixed layer to background values of $10^{-5}\,m^{-2}\,s^{-1}$ [*Whalen et al.*, 2012] using a 1/e scaling observed by *Sun et al.* [2013] from microstructure measurements (example decay profile, Figure 5). The model was run with both a uniform κ_z throughout the water column and the seasonally varying, enhanced κ_z at the boundary between the mixed layer and the box below.

At every time step, each flux in equation (2) is calculated and new oxygen concentration and saturation are determined for each box. For comparison with model output and to calculate ANCP, float data are binned into 2 week averages and interpolated to the model time and depth resolution. In addition to the flux calculations, the float measured $[O_2]$ (Figure 6a) was compared to modeled $[O_2]$ (Figure 6b) and evaluated at each time step to determine $d(h[O_2])/dt$ (left side of equation (2)). This represents the difference in

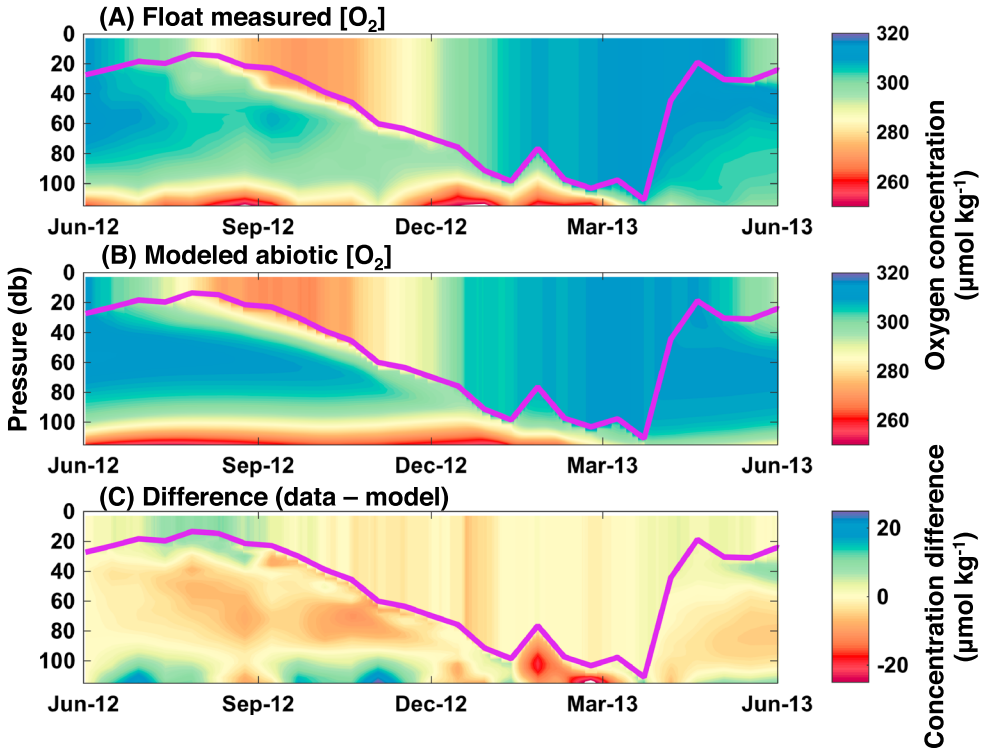

Figure 6. (a) Float measured $[O_2]$, (b) model-produced abiotic $[O_2]$, and (c) the difference as a function of pressure and time in the upper ocean for June 2012 to June 2013. Changes in $[O_2]$ throughout the year are largely controlled by solubility, with differences between the measured and modeled data showing areas of biological production and respiration. The difference (Figure 6c) between the measured and modeled $[O_2]$ is due to biological processes. Areas of high and low $[O_2]$ around 90–110 m are a combination of heaving isopycnals in the data that are not reproduced in the model and diffusion to low-oxygen waters below.

Table 1. Monte Carlo Error Analysis for the ANCP Model[a]

Parameter	Error (%)	ANCP Error (mol C m^{-2} yr^{-1})
Oxygen	0.1	±0.2
$F_{A\text{-}W}$	~26	±0.3
κ_{ML}	100	±0.1
κ_{Deep}	50	±0.2
P_{ATM}	0.5	±0.01
All	-	0.7 ± 0.5

[a]Each input term was varied with the standard deviation of the error matching the percent listed above. For example, the 0.1% error SD for the oxygen measurement means that for each Monte Carlo run the oxygen was varied according to a normal distribution with the mean equal to the measured value and a distribution such that 1 SD was equal to 0.1% of the mean pO_2. Errors are relative to and do not change the ANCP value of 0.7 mol C m^{-2} yr^{-1}. Monte Carlos for individual parameters were run 200 times, and total, with all parameters, was run through 1500 iterations. We used a constant value (ΔO_2:ΔOC = 1.45) to convert net biological oxygen production values into ANCP values.

oxygen storage between the measured data and model output (Figure 6c). J_{O_2} is integrated over the depth of the seasonal mixed layer (115 m) and over one annual cycle (June 2012 to June 2013). This approach differs from previous mass balance models at OSP because the abiotic model is run out a full year, including the winter months where supersaturations are close to zero.

2.3. Error Analysis

Monte Carlo error analyses were run for the most important flux contributors to the oxygen balance, both individually and together. Each parameter was varied around its measured or calculated value according to an input error that represents ± 1 standard deviation (SD) of the modeled uncertainty (Table 1). Two hundred iterations were performed for each individual flux and 1500 iterations for all errors simultaneously. Additional iterations did not alter the mean or SD of calculated ANCP. In *Wanninkhof* [2014], the total error in the air-sea gas flux is estimated as approximately ± 20%, which includes error in the wind speed. *Liang et al.* [2013] do not give an error estimate, but we assume that each component of $F_{A\text{-}W}$ (diffusive exchange, large bubbles, and small bubbles) contains a portion of the total error. We assigned a ± 15% error to each component of $F_{A\text{-}W}$; this assumes the errors are uncorrelated, which is unlikely but is a reasonable first estimate. The square root of the mean of the squared errors yields a total error of ± 26%, which gives a slightly more conservative estimate than *Wanninkhof* [2014].

Optode oxygen measurements in air allow calculation of the pO_2 difference between air and water. The air-water pO_2 difference drives the air-sea flux of oxygen and, because the same sensor is measuring both water and air, is independent of the optode calibration. Therefore, error in the oxygen measurements is due to our ability to measure the air-water difference. Uncertainty in the accuracy of the air measurements is approximately ± 0.1% (see supporting information for details of air measurement error).

The final significant source of error is the background diapycnal diffusivity coefficient. Error in the background κ_z (10^{-5} m^2 s^{-1}) is reported in *Ledwell et al.* [1993] as ± 20%. However, a wintertime κ_z estimate of 1.5×10^{-5} m^2 s^{-1} is reported as well. We chose an error of ± 50% for the background κ_z in the model. Error in mixed layer κ_z was taken from *Cronin et al.* [2015], which indicated a confidence bound for both heat and salt balance-derived κ_z climatologies of approximately the same order of magnitude as the derived diffusivity coefficients. We therefore chose an error of ±100% for the mixed layer κ_z.

3. Results and Discussion

3.1. ANCP Calculated From Float Data and Gas Model

The main feature in float measured ΔO_2 (Figure 1) is the strong supersaturation in and immediately below the mixed layer in summer (the surface depth interval indicated by the thick line in Figure 1), which gives way to near and slightly undersaturated water in the winter. Supersaturations vary from several percent above atmospheric equilibrium (positive values) in summer to less than 1% undersaturated in winter.

Measured oxygen (Figure 6a) and modeled abiotic oxygen (Figure 6b) are compared to determine the difference in oxygen concentration throughout the water column (Figure 6c). The difference represents the biologically produced oxygen stored in the water column, which, together with the difference in fluxes, represents the net biological oxygen production. Summertime production values (April–September only), which are most comparable to previous studies, yield ANCP of 2.0 ± 0.5 mol O_2 m^2 yr^{-1} (1.4 ± 0.4 mol C m^{-2} yr^{-1}, ΔO:C = 1.45, and ± 1 SD from Monte Carlo) by assuming no net production in winter (October–March). Estimates of ANCP based on the full year of data are lower, with a total of 1.0 ± 0.7 mol O_2 m^{-2} yr^{-1} (0.7 ± 0.5 mol C m^{-2} yr^{-1}), with wintertime respiration offsetting about half of the summer production.

Table 2. NCP Calculated With Increasing Model Complexity[a]

Mechanism	Summer (mol C m^{-2})	Annual (mol C m^{-2} yr^{-1})
$F_{A\text{-}W}$, no bubbles[b]	[f]	2.1
$F_{A\text{-}W}$, with bubbles[c]	[f]	0.1
$F_{A\text{-}W}$, bubbles + diapycnal mixing[d]		
$\kappa_z = 10^{-5}$ m^2 s^{-1}	1.5 ± 0.4	0.4 ± 0.4
κ_z based on heat/salt flux	1.3[e] ± 0.4	0.7 ± 0.5

[a]Calculating ANCP from O_2 data using progressively more complete terms in the abiotic model to illustrate the importance of different physical processes in evaluating the net biological O_2 production.
[b]Considering only the air-sea flux calculated from float data and a gas exchange parameterization that does not explicitly include bubbles [*Wanninkhof*, 2014];
[c]The same flux calculation using a gas exchange parameterization that includes bubbles [*Liang et al.*, 2013];
[d]Using the abiotic model described by equation (2) and two κ_z configurations: the first with a constant water column κ_z and the second with a κ_z that is enhanced at the base of the mixed layer and decays to the background κ_z of 10^{-5} m^2 s^{-1} 20 m below. Summertime values represent April–September.
[e]For these runs, horizontal and vertical advective fluxes were not included. Addition of the advective fluxes slightly increases summer production to 1.4 ± 0.4 mol C m^{-2} yr^{-1}.
[f]Calculated using data only and assume no net change in oxygen over an annual cycle. Summer values are not shown because these would represent an oxygen flux due to both biology and changes in solubility.

The importance of the different terms in the mass balance can be evaluated by successive estimates of ANCP using increasingly more realistic approaches to the calculation (Table 2). The simplest approach, and one that is unavoidable if one is dealing with a time series of surface ocean-only oxygen measurements [*Quay et al.*, 2012; *Juranek et al.*, 2012], is to assume that over the annual cycle there is no net change in oxygen content and that mixing and advection are unimportant, i.e., the first and last terms on the right-hand side of equation (1) must be equal. Using a gas exchange parameterization that does not explicitly include bubble processes [*Wanninkhof*, 2014] yields an inferred ANCP of 3.1 mol O_2 m^{-2} yr^{-1} (2.1 mol C m^{-2} yr^{-1}, row 1 of Table 2). Increasing the complexity of the calculation by including the gas exchange model of *Liang et al.* [2013], which incorporates explicit bubble fluxes, yields an ANCP of 0.2 mol O_2 m^{-2} yr^{-1} (0.1 mol C m^{-2} yr^{-1}). Both the models with and without bubbles result in similar outgassing of oxygen during the supersaturated summer months, but the model without bubbles predicts far less gas input from the atmosphere during the winter when high winds create bubbles that insert gases into the water. A greater flux of oxygen from the atmosphere due to bubbles results in a lower inferred biological production in order to match the observations.

Finally, including diapycnal eddy diffusion impacts the entire water column by removing oxygen according to the gradient at the depth of the winter mixed layer (~115 m). The oxygen gradient at this depth is negative (decreasing oxygen with increasing depth), so diapycnal eddy diffusivity removes oxygen from the upper water column. With no diapycnal eddy diffusion, influx from bubbles would nearly balance efflux from air-sea surface according to the previous discussion (ANCP = 0.1 mol C m^{-2} yr^{-1}). Employing a background value of the eddy diffusion coefficient ($\kappa_z = 10^{-5}$ m^2 s^{-1}) increases this value by 0.3 mol C m^{-2} yr^{-1}, and using diapycnal eddy diffusion at the base of the mixed layer determined from heat flux [*Cronin et al.*, 2015] (Figure 4) increases it to a total of 0.7 mol C m^{-2} yr^{-1} (Table 2 and Figure 7b).

The roughly equal importance of background κ_z and mixed layer κ_z is due to the seasonal cycle of the mixed layer depth. For most of the year the mixed layer is well above its deepest depth (~115 m), so the background κ_z is responsible for the slow diffusion of oxygen out of the upper ocean. κ_z at the base of the mixed layer is most important during the winter months, when the mixed layer comes into contact with deep, low-oxygen waters. Addition of horizontal and vertical advective fluxes to the model reduces the final calculated ANCP by a small but insignificant amount.

In summary, the most significant flux terms in the abiotic oxygen model are surface air-sea gas exchange, injection by bubbles, and the flux from diapycnal diffusion (Figure 7a). On an annual basis, diffusive gas exchange and diapycnal diffusion act to remove oxygen from the water column and are balanced by bubble fluxes and net biological production injecting oxygen into the upper ocean. Diffusive gas exchange exhibits a seasonal cycle that follows the mixed layer oxygen supersaturation. During summer months, high surface supersaturations and low wind speeds cause a strong flux out of the water column (negative values in Figure 7a) before winter undersaturation results in diffusion of oxygen back into the mixed layer. During the winter, with no bubble injection, the small diffusive flux of oxygen into the surface ocean would result in little inferred change in net biological production. With bubble injection, the large physical flux of oxygen

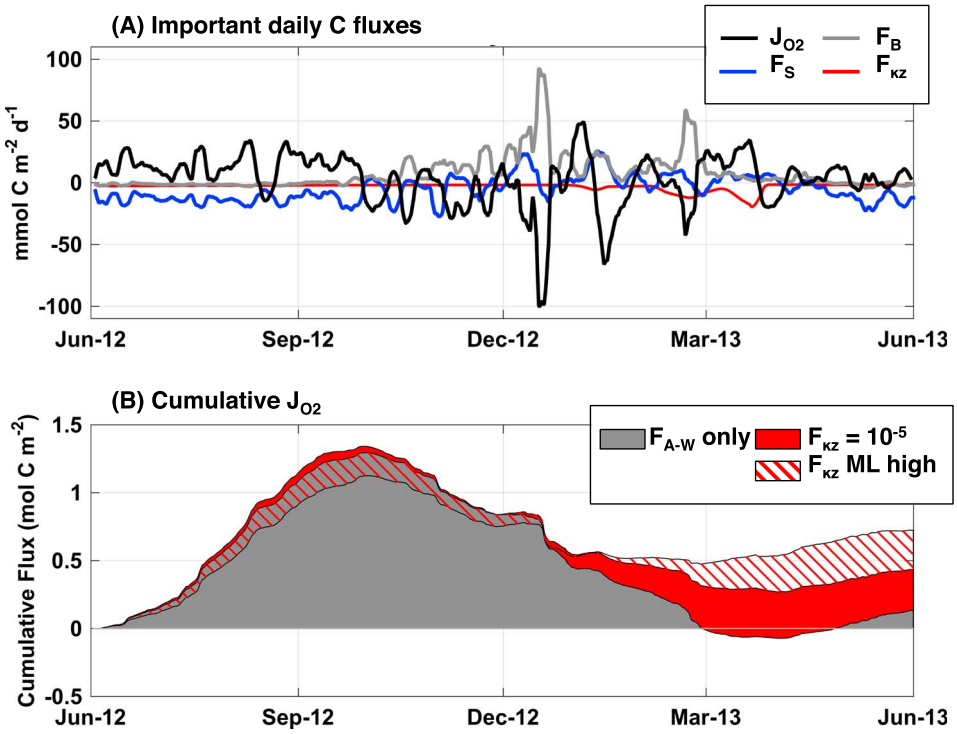

Figure 7. Daily and cumulative fluxes of carbon used to calculate upper ocean ANCP. (a) Modeled daily abiotic oxygen fluxes in units of carbon showing the most important terms and the calculated biological production, J_{O_2} (in units of C). Positive values represent addition of oxygen (organic carbon) to the ocean. Air-sea surface gas exchange (F_S) and bubble (F_B) fluxes are the constituent components of $F_{A\text{-}W}$. High winds and rapid atmospheric pressure can cause high, brief fluxes. For clarity, fluxes are smoothed using a 3 week running mean. (b) Cumulative biological production (J_{O_2}) for three model runs. Increasing values mean that biological oxygen is being produced in the upper ocean; flat indicates no change with time; and a downward trend marks a decrease in the flux. Values at the very end represent the annual magnitude of J_{O_2} for each model run.

into the water requires net respiration to maintain that same slightly undersaturated water. The largest source of error in this study is uncertainty in the air-sea gas flux (Table 1).

The small error for the oxygen sensor could not be achieved without in situ atmospheric calibration. The advantage of the in situ calibration of optodes to atmospheric oxygen is that it is possible to directly measure the air-water difference in oxygen, which determines the flux. Uncertainty in the initial oxygen calibration or in the atmospheric pressure estimate does not change the gas flux. As long as the same pressure product is used for both calibration and subsequent mass balance analysis, uncertainty in atmospheric pressure adds no error to the ANCP calculation.

3.2. Evaluation of ANCP Relative to Prior Estimates

Emerson [2014] compiled ANCP calculations at OSP from a variety of mass balance and sediment trap studies in addition to satellite- and model-based estimates. Both oxygen and nitrate mass balances suggested ANCP of 2.3 ± 0.6 mol C m^{-2} yr^{-1}. These values, however, used only data from the summer months and assumed the wintertime contribution was negligible. The net wintertime oxygen loss modeled in this study implies that respiration outweighs production at this time of the year, which has a significant impact on the annual carbon export.

Net heterotrophy during the winter at first seems to be in conflict with earlier sediment trap and thorium mass balance studies showing particle export throughout the year [*Charette et al.*, 1999; *Wong et al.*, 1999] with a total annual flux of 0.5 mol C m^{-2} yr^{-1} at 200 m [*Timothy et al.*, 2013]. However, it is possible that dissolved organic carbon (DOC) production can allow both year-round particle export and wintertime net heterotrophy. If a significant fraction of the summertime production is in the form of semilabile DOC, the net heterotrophy observed in this study during the winter could be driven by the consumption of

accumulated DOC even as low rates of autotrophy drive particle export. While there appear to be no studies of seasonal variability in surface DOC for the North Pacific subarctic ocean, the magnitude of seasonal change elsewhere has been reported as 5–30 μM [*Hansell and Carlson*, 2001]. We observe a decrease of ~1 mol O_2 m^{-2} (~0.7 mol C m^{-2}) from the summertime max to the wintertime low (Figure 7b). A decrease of this magnitude would require the respiration of approximately 9 μM DOC (assuming an average mixed layer depth of ~75 m during this time), which falls within the range of observed seasonal variability in epipelagic DOC.

Using an ecosystem model coupled to satellite derived chlorophyll and carbon, *Siegel et al*. [2014] arrive at a particulate organic carbon flux of approximately 2.5 mol C m^{-2} yr^{-1} for the northeastern subarctic gyre. This value agrees with the oxygen and nitrate mass balances compiled in *Emerson* [2014] but again is higher than the annual estimate from this study. Summertime rates of NCP are similar between our study and the satellite-predicted fluxes, thus differences in the winter NCP rates must account for the lower ANCP determined here. *Sonnerup et al*. [2013] used CFC-derived transit times and AOU along a North Pacific transect to calculate an organic carbon export of ~0.5 ± 0.2 mol C m^{-2} yr^{-1} at 50°N. This technique should integrate seasonal cycles in net production and is very close to the value we predict for the subarctic Pacific.

4. Conclusions

We used accurate, yearlong measurements of oxygen from a profiling float achieved by in situ calibration and an upper ocean model to determine annual net community production and the magnitude of the biological pump in the subarctic Pacific Ocean. Because we were able to determine accurate, frequent year-round flux estimates, it has been possible to show that there is net respiration during darker, less productive times of year. Interpretation of surface ocean oxygen measurements in terms of annual net community production requires an accurate model for bubble processes in regions where there are high winds in the wintertime. Furthermore, diapycnal diffusion of low-oxygen waters into the upper ocean is a significant term in the upper ocean oxygen mass balance.

Our results agree with independent latitudinal trends of the biological pump determined from apparent oxygen utilization rates evaluated with tracer age in the upper thermocline [*Sonnerup et al*., 2013] but are at odds with predictions from satellites and ocean global circulation models. The number and geographic distribution of experimentally determined measurements of the biological pump will have to be increased to accurately inform satellite and global circulation models of this essential biogeochemical boundary condition. This could be achieved by yearlong upper ocean oxygen mass balances determined from in situ measurements on remote platforms.

Acknowledgments

Float data are available in the online supporting information. Mooring gas tension device data, shipboard Winkler measurements, and model code are available upon request from the authors. We thank Stephen Riser and Dana Swift for their assistance in development of the O_2-Argo float and Marie Robert, Doug Yelland, Michael Craig, Jennifer Keene, Meghan Cronin, and the crew of the CCGS *John P. Tully* for assistance in deploying the float and mooring at OSP. We would also like to thank Noel Pelland for insightful comments throughout the development of the upper ocean abiotic gas model. This work was supported by a National Science Foundation grant OCE-1129112 and a National Science Foundation IGERT fellowship.

References

Altabet, M. A. (2007), Constraints on oceanic N balance/imbalance from sedimentary ^{15}N records, *Biogeosciences*, *4*(1), 75–86, doi:10.5194/bg-4-75-2007.

Bentamy, A., D. Croize-Fillon, and C. Perigaud (2008), Characterization of ASCAT measurements based on buoy and QuikSCAT wind vector observations, *Ocean Sci.*, *4*(4), 265–274, doi:10.5194/os-4-265-2008.

Bittig, H. C., and A. Körtzinger (2015), Tackling oxygen optode drift: Near-surface and in-air oxygen optode measurements on a float provide an accurate in-situ reference, *J. Atmos. Oceanic Technol.*, *32*, 1536–1543, doi:10.1175/JTECH-D-14-00162.1.

Bopp, L., et al. (2013), Multiple stressors of ocean ecosystems in the 21st century: Projections with CMIP5 models, *Biogeosciences*, *10*(10), 6225–6245, doi:10.5194/bg-10-6225-2013.

Bushinsky, S. M., and S. Emerson (2013), A method for in-situ calibration of Aanderaa oxygen sensors on surface moorings, *Mar. Chem.*, *155*, 22–28, doi:10.1016/j.marchem.2013.05.001.

Charette, M. A., S. B. Moran, and J. K. B. Bishop (1999), 234 Th as a tracer of particulate organic carbon export in the subarctic northeast Pacific Ocean, *Deep Sea Res., Part II*, *46*, 2833–2861.

Cronin, M. F., N. Pelland, S. Emerson, and W. R. Crawford (2015), Estimating diffusivity from the mixed layer heat and salt balances in the North Pacific, *J. Geophys. Res. Oceans*, doi:10.1002/2015JC011010.

D'Asaro, E. A., and C. McNeil (2013), Calibration and stability of oxygen sensors on autonomous floats, *J. Atmos. Oceanic Technol.*, *30*(8), 1896–1906, doi:10.1175/JTECH-D-12-00222.1.

de Boyer Montégut, C., G. Madec, A. S. Fischer, A. Lazar, and D. Iudicone (2004), Mixed layer depth over the global ocean: An examination of profile data and a profile-based climatology, *J. Geophys. Res.*, *109*, C12003, doi:10.1029/2004JC002378.

Diaz, R. J., and R. Rosenberg (2008), Spreading dead zones and consequences for marine ecosystems, *Science*, *321*, 926–929, doi:10.1126/science.1156401.

Emerson, S. (2014), Annual net community production and the biological carbon flux in the ocean, *Global Biogeochem. Cycles*, *28*, 14–28, doi:10.1002/2013GB004680.

Emerson, S., and C. Stump (2010), Net biological oxygen production in the ocean—II: Remote in situ measurements of O_2 and N_2 in subarctic Pacific surface waters, *Deep Sea Res., Part I*, *57*(10), 1255–1265, doi:10.1016/j.dsr.2010.06.001.

Emerson, S., C. Stump, and D. Nicholson (2008), Net biological oxygen production in the ocean: Remote in situ measurements of O_2 and N_2 in surface waters, *Global Biogeochem. Cycles*, *22*, GB3023, doi:10.1029/2007GB003095.
Emerson, S. R., and S. M. Bushinsky (2014), Oxygen concentrations and biological fluxes in the open ocean, *Oceanography*, *27*(1), 168–171.
Fiedler, B., P. Fietzek, N. Vieira, P. Silva, H. C. Bittig, and A. Körtzinger (2013), In situ CO_2 and O_2 measurements on a profiling float, *J. Atmos. Oceanic Technol.*, *30*(1), 112–126, doi:10.1175/JTECH-D-12-00043.1.
García, H. E., and L. I. Gordon (1992), Oxygen solubility in seawater: Better fitting equations, *Limnol. Oceanogr.*, *37*(6), 1307–1312.
Garcia, H. E., R. A. Locarnini, T. P. Boyer, J. I. Antonov, O. K. Baranova, M. M. Zweng, and D. R. Johnson (2010), *World Ocean Atlas 2009*, *Dissolved Oxygen, Apparent Oxygen Utilization, and Oxygen Saturation.*, *NOAA Atlas NESDIS 70*, vol. 3, 344 pp., U.S. Gov. Print. Off., Washington, D. C.
Gruber, N., S. C. Doney, S. R. Emerson, D. Gilbert, T. Kobayashi, A. Körtzinger, G. C. Johnson, K. S. Johnson, S. C. Riser, and O. Ulloa (2009), Adding oxygen to Argo: Developing a global in-situ observatory for ocean deoxygenation and biogeochemistry, paper presented at Ocean Obs '09.
Hansell, D. A., and C. A. Carlson (2001), Marine dissolved organic matter and the carbon cycle, *Oceanography*, *14*(4), 41–49.
Hartmann, D. L. (1994), The ocean general circulation and climate, in *Global Physical Climatology*, pp. 171–203, Academic Press, San Diego, Calif.
Hofmann, M., and H.-J. Schellnhuber (2009), Oceanic acidification affects marine carbon pump and triggers extended marine oxygen holes, *Proc. Natl. Acad. Sci. U.S.A.*, *106*(9), 3017–3022, doi:10.1073/pnas.0813384106.
Johnson, K. S., W. M. Berelson, E. S. Boss, Z. Chase, H. Claustre, S. R. Emerson, N. Gruber, A. Körtzinger, M. J. Perry, and S. C. Riser (2009), Observing biogeochemical cycles at global scales with profiling floats and gliders: Prospects for a global array, *Oceanography*, *22*(3), 216–225.
Juranek, L. W., P. D. Quay, R. A. Feely, D. Lockwood, D. M. Karl, and M. J. Church (2012), Biological production in the NE Pacific and its influence on air-sea CO_2 flux: Evidence from dissolved oxygen isotopes and O_2/Ar, *J. Geophys. Res.*, *117*, C05022, doi:10.1029/2011JC007450.
Kalnay, E., et al. (1996), The NCEP/NCAR 40-year reanalysis project, *Bull. Am. Meteorol. Soc.*, *77*, 437–471, doi:10.1175/1520-0477(1996)077<0437:TNYRP>2.0.CO;2.
Kwon, E. Y., F. Primeau, and J. L. Sarmiento (2009), The impact of remineralization depth on the air-sea carbon balance, *Nat. Geosci.*, *2*(9), 630–635, doi:10.1038/ngeo612.
Laws, E. A., E. D'Sa, and P. Naik (2011), Simple equations to estimate ratios of new or export production to total production from satellite-derived estimates of sea surface temperature and primary production, *Limnol. Oceanogr. Methods*, *9*(1979), 593–601, doi:10.4319/lom.2011.9.593.
Ledwell, J. R., A. J. Watson, and C. S. Law (1993), Evidence for slow mixing across the pycnocline from an open-ocean tracer-release experiment, *Nature*, *364*, 701–703, doi:10.1038/364701a0.
Liang, J.-H., C. Deutsch, J. C. McWilliams, B. Baschek, P. P. Sullivan, and D. Chiba (2013), Parameterizing bubble-mediated air-sea gas exchange and its effect on ocean ventilation, *Global Biogeochem. Cycles*, *27*, 894–905, doi:10.1002/gbc.20080.
Munro, D. R., P. D. Quay, L. W. Juranek, and R. Goericke (2013), Biological production rates off the Southern California coast estimated from triple O_2 isotopes and O_2: Ar gas ratios, *Limnol. Oceanogr.*, *58*(4), 1312–1328.
Nicholson, D., S. Emerson, and C. C. Eriksen (2008), Net community production in the deep euphotic zone of the subtropical North Pacific gyre from glider surveys, *Limnol. Oceanogr.*, *53*(5 part 2), 2226–2236, doi:10.4319/lo.2008.53.5_part_2.2226.
Quay, P., J. Stutsman, and T. Steinhoff (2012), Primary production and carbon export rates across the subpolar N. Atlantic Ocean basin based on triple oxygen isotope and dissolved O_2 and Ar gas measurements, *Global Biogeochem. Cycles*, *26*, GB2003, doi:10.1029/2010GB004003.
Riser, S. C., and K. S. Johnson (2008), Net production of oxygen in the subtropical ocean, *Nature*, *451*(January), 323–326, doi:10.1038/nature06441.
Siegel, D. A., K. O. Buesseler, S. C. Doney, S. F. Sailley, M. J. Behrenfeld, and P. W. Boyd (2014), Global assessment of ocean carbon export by combining satellite observations and food-web models, *Global Biogeochem. Cycles*, *28*, 181–196, doi:10.1002/2013GB004743.
Sonnerup, R. E., S. Mecking, and J. L. Bullister (2013), Transit time distributions and oxygen utilization rates in the Northeast Pacific Ocean from chlorofluorocarbons and sulfur hexafluoride, *Deep Sea Res., Part I*, *72*, 61–71, doi:10.1016/j.dsr.2012.10.013.
Sun, O. M., S. R. Jayne, K. L. Polzin, B. A. Rahter, and L. C. St. Laurent (2013), Scaling turbulent dissipation in the transition layer, *J. Phys. Oceanogr.*, *43*(11), 2475–2489, doi:10.1175/JPO-D-13-057.1.
Takeshita, Y., T. R. Martz, K. S. Johnson, J. N. Plant, D. Gilbert, S. C. Riser, C. Neill, and B. Tilbrook (2013), A climatology-based quality control procedure for profiling float oxygen data, *J. Geophys. Res. Oceans*, *118*, 5640–5650, doi:10.1002/jgrc.20399.
Timothy, D. A., C. S. Wong, J. E. Barwell-Clarke, J. S. Page, L. A. White, and R. W. Macdonald (2013), Climatology of sediment flux and composition in the subarctic Northeast Pacific Ocean with biogeochemical implications, *Prog. Oceanogr.*, *116*, 95–129, doi:10.1016/j.pocean.2013.06.017.
Toggweiler, J. R., and J. L. Sarmiento (1985), Glacial to interglacial changes in atmospheric carbon dioxide: The critical role of ocean surface water in high latitudes, in *The Carbon Cycle and Atmospheric CO_2: Natural Variations Archean to Present*, edited by E. T. Sundquist and W. S. Broecker, pp. 163–184, AGU, Washington, D. C.
Volk, T., and Z. Liu (1988), Controls of CO_2 sources and sinks in the Earth scale surface ocean: Temperature and nutrients, *Global Biogeochem. Cycles*, *2*, 73–89, doi:10.1029/GB002i002p00073.
Wanninkhof, R. (2014), Relationship between wind speed and gas exchange over the ocean revisited, *Limnol. Oceanogr. Methods*, *12*, 351–362, doi:10.4319/lom.2014.12.351.
Westberry, T. K., P. J. L. B. Williams, and M. J. Behrenfeld (2012), Global net community production and the putative net heterotrophy of the oligotrophic oceans, *Global Biogeochem. Cycles*, *26*, GB4019, doi:10.1029/2011GB004094.
Whalen, C. B., L. D. Talley, and J. A. MacKinnon (2012), Spatial and temporal variability of global ocean mixing inferred from Argo profiles, *Geophys. Res. Lett.*, *39*, L18612, doi:10.1029/2012GL053196.
Wong, C. S., F. A. Whitney, D. W. Crawford, K. Iseki, R. J. Matear, W. K. Johnson, J. S. Page, and D. Timothy (1999), Seasonal and interannual variability in particle fluxes of carbon, nitrogen and silicon from time series of sediment traps at Ocean Station P, 1982–1993: Relationship to changes in subarctic primary productivity, *Deep Sea Res., Part II*, *46*, 2735–2760.
Yool, A., E. E. Popova, and T. R. Anderson (2013), MEDUSA-2.0: An intermediate complexity biogeochemical model of the marine carbon cycle for climate change and ocean acidification studies, *Geosci. Model Dev.*, *6*, 1767–1811, doi:10.5194/gmd-6-1767-2013.